Appl Biochem Biotechnol (2016) 178:1534–1545
DOI 10.1007/s12010-015-1966-7

Exploring the Effects of Subfreezing Temperature and Salt Concentration on Ice Growth Inhibition of Antarctic Gram-Negative Bacterium *Marinomonas Primoryensis* Using Coarse-Grained Simulation

Hung Nguyen[1] · **Thanh Dac Van**[1,2] · **Nhut Tran**[1] · **Ly Le**[1,2]

Received: 16 November 2015 / Accepted: 21 December 2015 /
Published online: 12 January 2016

Abstract The aim of this work is to study the freezing process of water molecules surrounding Antarctic Gram-negative bacterium *Marinomonas primoryensis* antifreeze protein (*Mp*AFP) and the *Mp*AFP interactions to the surface of ice crystals under various marine environments (at different NaCl concentrations of 0.3, 0.6, and 0.8 mol/l). Our result indicates that activating temperature region of *Mp*AFPs reduced as NaCl concentration increased. Specifically, *Mp*AFP was activated and functioned at 0.6 mol/l with temperatures equal or larger 278 K, and at 0.8 mol/l with temperatures equal or larger 270 K. Additionally, *Mp*AFP was inhibited by ice crystal network from 268 to 274 K and solid–liquid hybrid from 276 to 282 K at 0.3 mol/l concentration. Our results shed lights on structural dynamics of *Mp*AFP among different marine environments.

Keywords MARTINI force field · *Mp*AFPs · Coarse-grained simulation · Free energy landscape

Introduction

Organisms living in subfreezing regions have acquired the ability to resist extreme cold conditions by producing antifreeze proteins (AFPs) which can inhibit ice crystal formation

✉ Hung Nguyen
hung.nv@icst.org.vn

✉ Ly Le
ly.le@hcmiu.edu.vn

[1] Life Science Laboratory of Institute for Computational Science and Technology, Ho Chi Minh City, Vietnam

[2] School of Biotechnology of Ho Chi Minh International University, Vietnam National University, Ho Chi Minh City, Vietnam

process. AFPs are composed of only protein or in combination with glycan via covalent bonds, also called antifreeze glycoprotein (AFGP) [1–3]. AFPs protect their host by limiting the growth of ice crystal inside and outside body fluids [4, 5]. AFPs and AFGPs have been found in various Antarctic organism including fish [6–8], plants [9–11], insects [12–15], fungi [16], and bacteria [3, 17–19]. The antifreeze mechanism of AFPs was determined through microscopic analysis which showed that AFPs bind to ice surface and prevent ice crystallization process. The difference between AFPs' melting point and freezing point is known as thermal hysteresis (TH), an important antifreeze indicator of different AFPs. In addition, AFPs at interface between solid ice and liquid water inhibit the thermodynamically favored growth of the ice crystal. Previous study showed that ice growth is kinetically inhibited by AFPs covering the water accessible surfaces of ice [20]. As TH can be measured in laboratory condition with a nanoliter osmometer [21], TH value of various AFPs was determined such as fish (0.7–1.5 °C), plants (0.2–0.5 °C), insects (3–6 °C), and bacteria (less than 0.1 °C) [22]. Bacterial AFPs were found to have the lowest TH value and first demonstrated by Duman and Olsen [3, 23]. AFPs are particularly sensitive to cooling condition as their molecular adaptation to ice crystal is induced through the gradual formation of ice cascade surrounding AFP which can also be interpreted as AFPs can be inactivated if subfreezing temperature suddenly drops [24].

The binding site of AFPs has been found to be relatively hydrophobic and also contained many potential hydrogen bond donors/acceptors. The idea of hydrogen bonds and the hydrophobic effects contribute to ice binding has been under investigation in recent decades [25, 26]. Hydrogen bonds were originally proposed to be the major interaction between AFPs and ice crystal [27]. However, this hypothesis failed to provide a rational explanation on how an AFP would preferably bind ice crystal. On the other hand, recent studies proposed that the hydrophobic effect could have played an important function in the ice inhibition process and provided with evidence that clathrate-like water on the hydrophobic ice-binding site (IBS) was found to be released into the solvent upon ice binding, resulting in a gain in entropy [28, 29]. In addition, molecular dynamics simulation studies indicated that the relatively hydrophobic IBS of AFPs is capable of reordering water molecules into an ice-like lattice and, instead of shedding bound water molecules upon ice binding, the reordered water molecules might facilitate the AFP's interaction with ice by matching certain ice geometrical planes [30]. Although intriguing as it seems, these simulations failed to describe the molecular mechanism explaining how an AFP acquires the ability to reorder water molecules in which binding specificity and affinity can assist in the irreversible absorption of AFP into forming ice lattices. These problems have been elucidated by the ice-binding mechanisms and the first crystal structure of Antarctic bacterium AFPs. The largest AFP experimental structures demonstrated that folds or Ca^{2+}-bound parallel beta-helices with an extensive array of ice-like surface waters were directly anchored via hydrogen bonds to the polypeptide backbone and the adjacent side chains [26, 30–36].

In recent study, Shuaiqi Guo and colleagues found a Ca^{2+}-dependent protein with molecular density of 1.5-MDa has particular ice-binding property, called *Marinomonas primoryensis* antifreeze protein (*Mp*AFP). This protein has five non-ice-binding regions, in which on ice-binding region II or RII constitutes approximately 90 % of its content and includes around 120 tandem repeats of 104-residue sequence. Furthermore, Ca^{2+} ion was found to be essential for RII monomer folding with Ca^{2+}/protein molar ratio of 10:1. Phase information of RII crystal structure monomer was determined with a resolution of 1.35 Å by single-wavelength anomalous dispersion and molecular replacement methods with Ca^{2+} as the heavy atom. The RII

monomer folding is similar to Ca^{2+}-bound immunoglobulin-like β-sandwich. Interestingly, the Ca^{2+} ions are coordinated at the interface between each RII monomer and its symmetry-related molecules, suggesting that these ions may involve in the stabilization of RII. The proposed role of RII is to help the aerobic bacterium bind to surface ice in an Antarctic lake in order to improve oxygen and nutrients accessibility [37].

The concentration of NaCl greatly affects the crystallization process of sea water. Since NaCl dissociate the ice crystal by positively charged Na^{+} ion and negatively charged Cl^{-} ion, the NaCl concentration then will keep the water under liquid form when temperature reaches lower than freezing point of °C. And NaCl concentration may vary dependent on chronological and geographical condition and distribution. From the thermodynamic point of view, the increase in NaCl concentration and anti-freezing mechanism of AFPs reduce ice crystallization process, respectively, as such was found in AFPs. This leads to the assumption that the change in NaCl concentration may have a certain degree of impact on the behavior and activity of *Mp*AFP. Therefore, in order to capture the full picture of *Mp*AFP anti-freezing mechanism, our objectives of this study were set to characterize the effects and the inhibiting ability of *Mp*AFP under freezing process in which different marine environments were incorporated by using different NaCl concentrations of 0.3, 0.6, and 0.8 mol/l using coarse-grained simulation.

Materials and Methods

Simulated System Preparation The 3D structure of *Mp*AFP was taken from Protein Data Bank (PDB) with PDB entry 4KDV [37]. We used Visual Molecular Dynamics (VMD) software [38] to show the structure of atomistic structure and then MARTINIZE version 2.2 to convert atomistic structure existing in PDB format into coarse-grained beads [39, 40]. Here, each amino acid was modeled by one or two beads according to their specific sizes, which has been classified into two broad categories: backbone and side chain beads.

Simulation Methods The GROMACS 4.5.5 package [41] with MARTINI force field for coarse-grained model were used to run MD simulation. The periodic boundary conditions were used throughout the simulation process; the electrostatic potential was shifted from 0.0 to 1.2 nm and the Lennard Jones (LJ) potential was shifted from 0.9 to 1.2 nm on all three axes (x, y, and z) [42]. The complexes were positioned inside a cubic box at a distance of 1.2 nm from the solute to the box surface and water model was used specifically in coarse-grained water model [43]:

– The melting point of water models used in MD simulation was not near to real water molecules [44, 45]. Such as the melting temperature of ice I(h) for several commonly used models of water (SPC, SPC/E, TIP3P, TIP4P, TIP4P/Ew, and TIP5P) obtained from computer simulations at $p = 1$ bar. Since the melting temperature of ice I(h) for the TIP4P model is now known [46], it is possible to use the Gibbs–Duhem methodology [47] to evaluate the melting temperature of ice I(h) for other potential models of water. Previous studies found that the melting temperatures of ice I(h) for SPC, SPC/E, TIP3P, TIP4P, TIP4P/Ew, and TIP5P models were 190, 215, 146, 232, 245, and 274 K, respectively. In this research, the coarse-grained water model is represented as one of the major simplification of the solvent, which can be implicitly or explicitly modeled as a van der Waals particle. In this water model, the effect of polarization and the proper screening of interactions depending on the local environment is

absent. In addition, the polarizable coarse-grained water molecules are represented by three particles instead of one as in the standard Martini force field. The central particle W is neutral and interacts with other particles in the system under the influence of the LJ potentials which depicts standard water molecules. The additional particles WP and WM are bound to the central particle and carry a positive and negative charge of $+q$ and $-q$, respectively. They interact with other particles via Coulomb function, and lack of LJ interactions. The bonds W-WP and W-WM are constrained to a particular distance and are symbolized as character *l*. In addition, the interactions between WP and WM particles inside the same coarse-grained water bead are excluded making these particles "transparent" to each other. In turn, the charged particles can rotate around the W particle. The dipole momentum of the water bead depends on the position of the charged particles and can vary from zero (charged particles coincide) to $2lq$ (charged particles at the maximal distance). A harmonic angle potential with equilibrium angle θ and force constant K_θ was added to control the rotation of WP and WM particles which in turn adjust the distribution of the dipole momentum. The average dipole momentum of the water bead is dependent on the charge distribution and was set to be on average zero in an apolar environment, such as the interior of the lipid bilayer. In contrast, some of non-zero average dipole were observed in bulk water or in other polar environments. The mass of the charged particles as well as the mass of the central particle was set to 24 amu and summed up to 72 amu (the mass of four real water molecules) [43].

– The properties of water model in MD simulation were carefully considered since water molecules play an important function as ubiquitous solvent in biological systems. In this research, the parameterization of polarizable coarse-grained water model was used in combination with the coarse-grained MARTINI force field. The three bead model representing four water molecules was used to show the effective accountability of real water-oriented polarity. Consequently, the dielectric screening of bulk water was reproduced. At the same time, the parameterization was used as water model with bulk water density and oil/water partitioning data which reproduced a similar level of accuracy as in the standard MARTINI force field.

The steepest descent simulation for minimization was performed over 50,000 steps. The equilibration was performed for 3 ns at temperature of 303 K using the Berendsen algorithm [48] and 1 bar constant pressure with the damping coefficient of 0.1 ps of the Parrinello–Rahman pressure [49]. The structures were generated as the configurations for our MD simulation with eight temperatures including 268, 270, 272, 274, 276, 278, 280, and 282 K. The final MD simulation allowed us to integrate the equations of motion with a time step of 2 fs and our simulation run for totally 100 ns in the leap-frog algorithm [50].

Free Energy Landscape Calculations Free energy landscape is a method used to point out possible conformations of a molecular entity, or the spatial positions of interacting molecules in a system, and their corresponding energy levels. In this research, local minimum of an energy landscape corresponding to metastable low temperature states of a thermodynamic system was used to determine representative trajectories by identifying the local minimum energy regions of free energy landscapes. The local minimum was defined by n-dimensional reaction coordinate $V=(V_1,\ldots,V_n)$ and was calculated using the function: $\Delta G(V)=-k_BT[\ln P(V)-\ln P_{max}]$, where $P(V)$ represents the probability distribution and P_{max} represents the maximum of the distribution, which was subtracted to $\Delta G=0$ for lowest free energy minimum [51, 52].

Results and Discussions

As shown in Fig. 1, the total energies (E_{tot} is included the kinetic and potential terms of energy) of *Mp*AFPs system were represented as a function of time. We used the variation in total energy of *Mp*AFPs systems at subfreezing temperatures to determine their dependence on temperature and NaCl concentration. This result indicates physical state transformation from liquid to solid of water molecules in the simulated complexes when subfreezing temperatures were set from 268 to 282 K and under different NaCl concentrations (NaCl concentrations were set to 0.3, 0.6, and 0.8 mol/l). At 268 K, water molecules surrounding *Mp*AFP were observed to transform from liquid solution to completely frozen in 0.3, 0.6, and 0.8 mol/l. From 270 to 274 K, we found that water molecules surrounding *Mp*AFP were frozen in both 0.3 and 0.6 mol/l concentrations; liquid form was observed at this temperature range in the case where NaCl concentration was 0.8 mol/l. At 276 K, water molecules surrounding *Mp*AFP became ice-liquid hybrid in 0.3 and 0.6 mol/l and liquid form in 0.8 mol/l. From 278 to 282 K, water molecules surrounding *Mp*AFP was ice-liquid hybrid in 0.3 mol/l while it remained in liquid form for both 0.6 and 0.8 mol/l. In addition, we also found that E_{tot} values of the complexes changed as NaCl concentrations changed. This resulted in physical state transformation (ice crystal or ice-liquid hybrid or liquid solution). In addition, E_{tot} value has a tendency to increase as NaCl concentration increased because of the effect of higher temperature conditions and ions are contributed to the change of kinetic energy lead to E_{tot} value is increased when NaCl concentration increased. Specifically, at 268 K, the ice state of treated complexes with different NaCl concentrations of 0.3, 0.6, and 0.8 mol/l were found to be different in term of E_{tot}. The total energy fluctuated around −62e + 03 (kJ/mol) in 0.3 and 0.6 mol/l, and around −59e + 03 (kJ/mol) in 0.8 mol/l; or along liquid form but the E_{tot} of complex simulated at 278 K fluctuated around −55e + 03 (kJ/mol) in 0.6 mol/l and −53e + 03 (kJ/mol) in 0.8 mol/l. Thus, the freezing process and energy states of the complexes were dependent upon NaCl concentration in marine environment. This means water solvent treated with low NaCl concentration environment can be frozen at higher temperature comparing to solvent treated with higher NaCl concentrations. Specifically, water molecules surrounding *Mp*AFPs were completely frozen from 268 to 274 K and ice-liquid hybrid from 276 to 282 K at 0.3 mol/l. On the other hand, water molecules surrounding

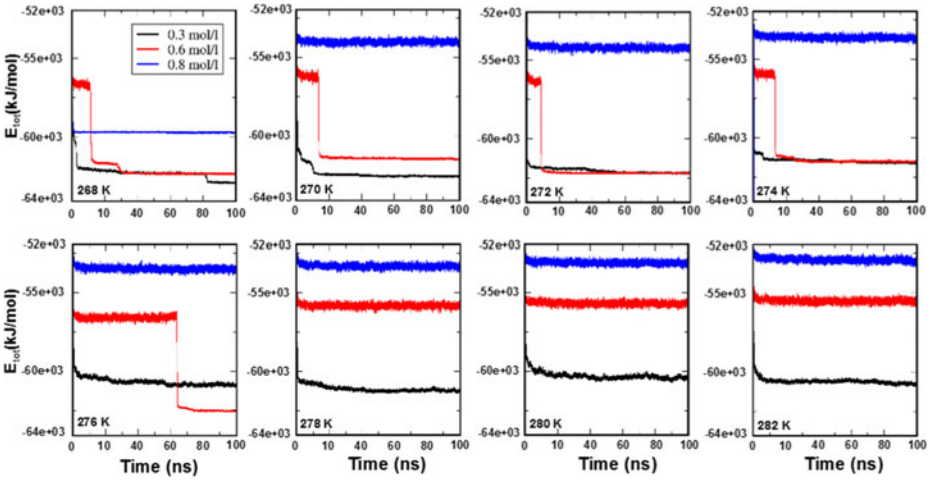

Fig. 1 The total energy E_{tot}(kJ/mol) of the *Mp*AFP systems at different NaCl concentrations of 0.3, 0.6, and 0.8 mol/l and different temperatures from 268 to 282 K

*Mp*AFPs at 0.6 mol/l were frozen from 268 to 274 K, ice-liquid at 276 K and existed in liquid state at temperatures of equal and greater than 278 K. Finally, for the simulated complexes with 0.8 mol/l, only the complex at 268 K was completely frozen, while the remaining complexes existed in liquid state. In sum, these results described the behaviors of water molecules surrounding *Mp*AFP at subfreezing temperature in which the formation and expansion of ice crystal led to the decrease of thermodynamic properties of the system and total energy of *Mp*AFPs systems.

As seen from Fig. 2, the radial distribution function was further used to describe the behavior of water molecules surrounding *Mp*AFP under subfreezing condition. The radial distribution functions were measured to analyze the distances of water molecules that come into contact with *Mp*AFP. The measurement was represented by the $g_{ww}(r)$ values or distances between water molecules surrounding *Mp*AFP. The $g_{ww}(r)$ tended to increase in peak number and height when water molecules surrounding *Mp*AFP formed ice crystal or ice-liquid hybrid. The $g_{ww}(r)$ was used to identify temperature regions of water molecules surrounding *Mp*AFP at different states (ice crystal or ice-liquid hybrid or liquid) and subsequently its activity under subfreezing condition. Figure 2 showed the $g_{ww}(r)$ of water molecules surrounding *Mp*AFP at different temperatures in different marine environments (with NaCl concentrations of 0.3, 0.6, and 0.8 mol/l). At 268 K, the $g_{ww}(r)$ fluctuated around 5 (r) for first peak, 2.3 (r) for second peak, 1.85 (r) for third peak, and 1(r) for fourth peak for all of three NaCl concentrations. This means water molecules surrounding *Mp*AFP were completely frozen for all three NaCl concentrations and that *Mp*AFP was not able to inhibit ice formation process. From 270 to 274 K, the $g_{ww}(r)$ value of water molecules surrounding *Mp*AFP in 0.8 mol/l fluctuated around the first peak (3.9 (r)), the second peak (1.5 (r)), and the third peak (1.3 (r)) while the $g_{ww}(r)$ values of water molecules surrounding *Mp*AFP in 0.3 and 0.6 mol/l were not changed comparing to the complex simulated at 268 K. At these temperatures, the water

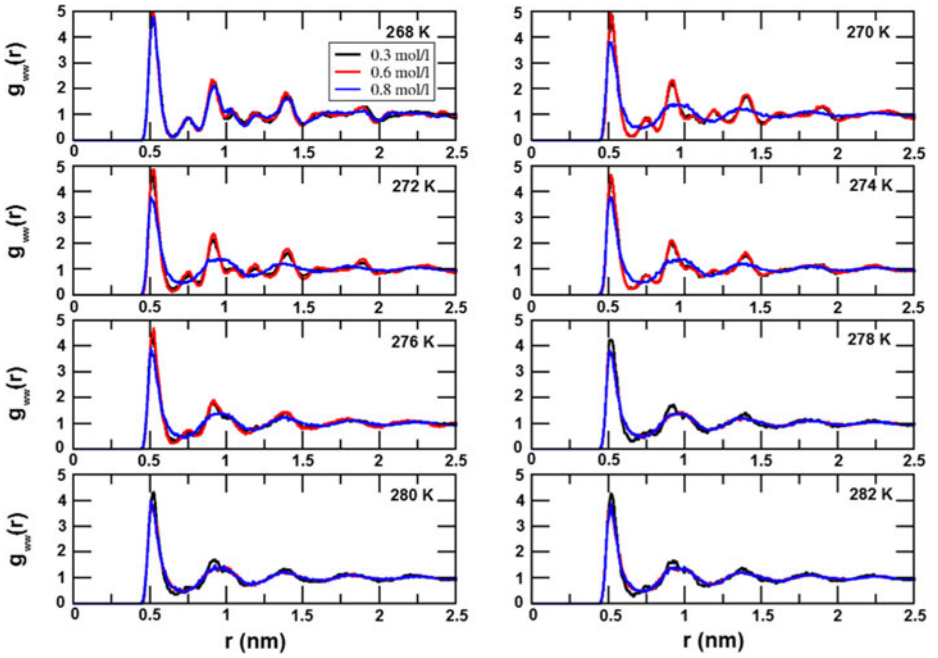

Fig. 2 The radial distribution function (RDF) $g_{ww}(r)$ of water–water at NaCl concentrations of 0.3, 0.6, and 0.8 mol/l at different temperatures from 268 to 282 K. Here r is the distance between water–water molecules

molecules surrounding *Mp*AFP existed in solid state at 0.3 and 0.6 mol/l and existed in liquid state at 0.8 mol/l. At 276 K, the peak height of the water $g_{ww}(r)$ surrounding *Mp*AFP at 0.3 and 0.6 mol/l were higher than at 0.8 mol/l. Such phenomenon occurred when the water molecules surrounding *Mp*AFP at 0.3 and 0.6 mol/l existed in ice-liquid hybrid form while in 0.8 mol/l existed in liquid form. From 278 to 282 K, water molecules surrounding *Mp*AFP were found to form ice-liquid hybrid at 0.3 mol/l and liquid solution at 0.6 and 0.8 mol/l.

The bond-oriented order parameters was also used as a method to determine the crystalline structure of liquid compound when which is changed from liquid to solid transition. The idea of the bond order parameters is to capture the symmetry of bond orientations regardless of the bond lengths. The bond was defined as the vector joining a pair of neighboring atoms. And the neighboring atoms of a given atom as those atoms which have an interatomic distance less than a cutoff radius of 3.5 Å, equal to the distance to the minimum between the first and the second peaks of the pair correlation function [53]. Based on the bond-oriented order parameter profiles, the results in Fig. 3 show that:

(a) For the complexes in 0.3 mol/l, the Fig. 3a showed that water molecules surrounding *Mp*AFP was completely frozen at 268 to 274 K and in ice-liquid hybrid form from 276 to 282 K.
(b) For the complexes in 0.6 mol/l, the Fig. 3b showed that water molecules surrounding *Mp*AFPs was completely frozen from 268 to 274 K and ice-liquid hybrid at 276 K. With the temperatures of equal and greater than 278 K, the water molecules surrounding *Mp*AFP was in liquid solution.
(c) For the complexes in 0.8 mol/l, the Fig. 3c showed that water molecules surrounding *Mp*AFP was mostly frozen at 268 K. It was in liquid format temperatures of equal and greater than 270 K.

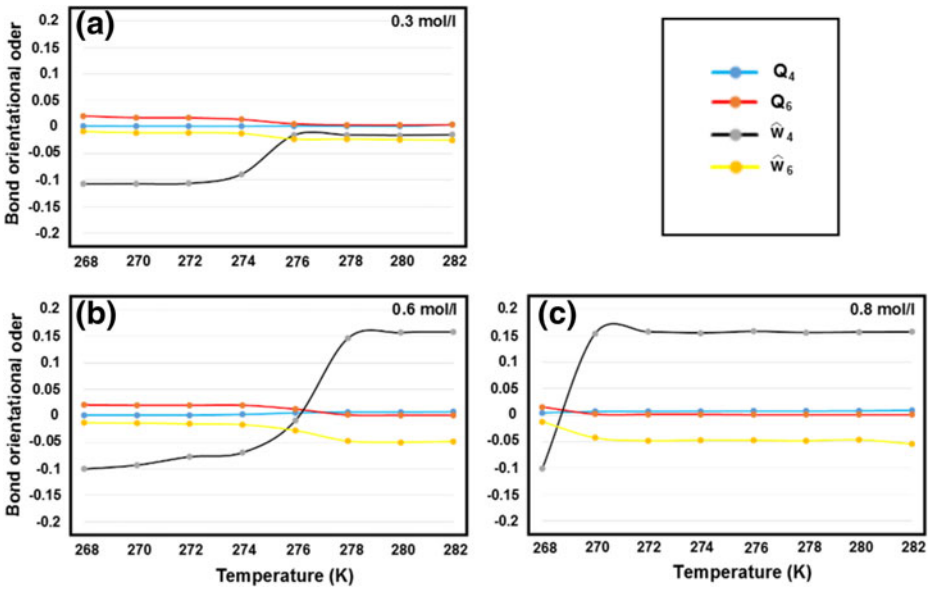

Fig. 3 The profile of the globally averaged bond-orientation order parameter vs the temperatures. Here, the Q_4, Q_6, $\hat{W}_4$, $\hat{W}_6$ were corresponding to the four bond order parameters to identify different crystal structures

Figures 4 and 5 showed the free energy landscape of all complexes, which allowed us to establish fundamental understanding on the interaction between water molecules and ice-binding site of *Mp*AFP at subfreezing temperatures using local minimum energy as indicator (in which *x* axis represents the radius of gyration (Rg) and *y* axis represents the root mean-square deviation

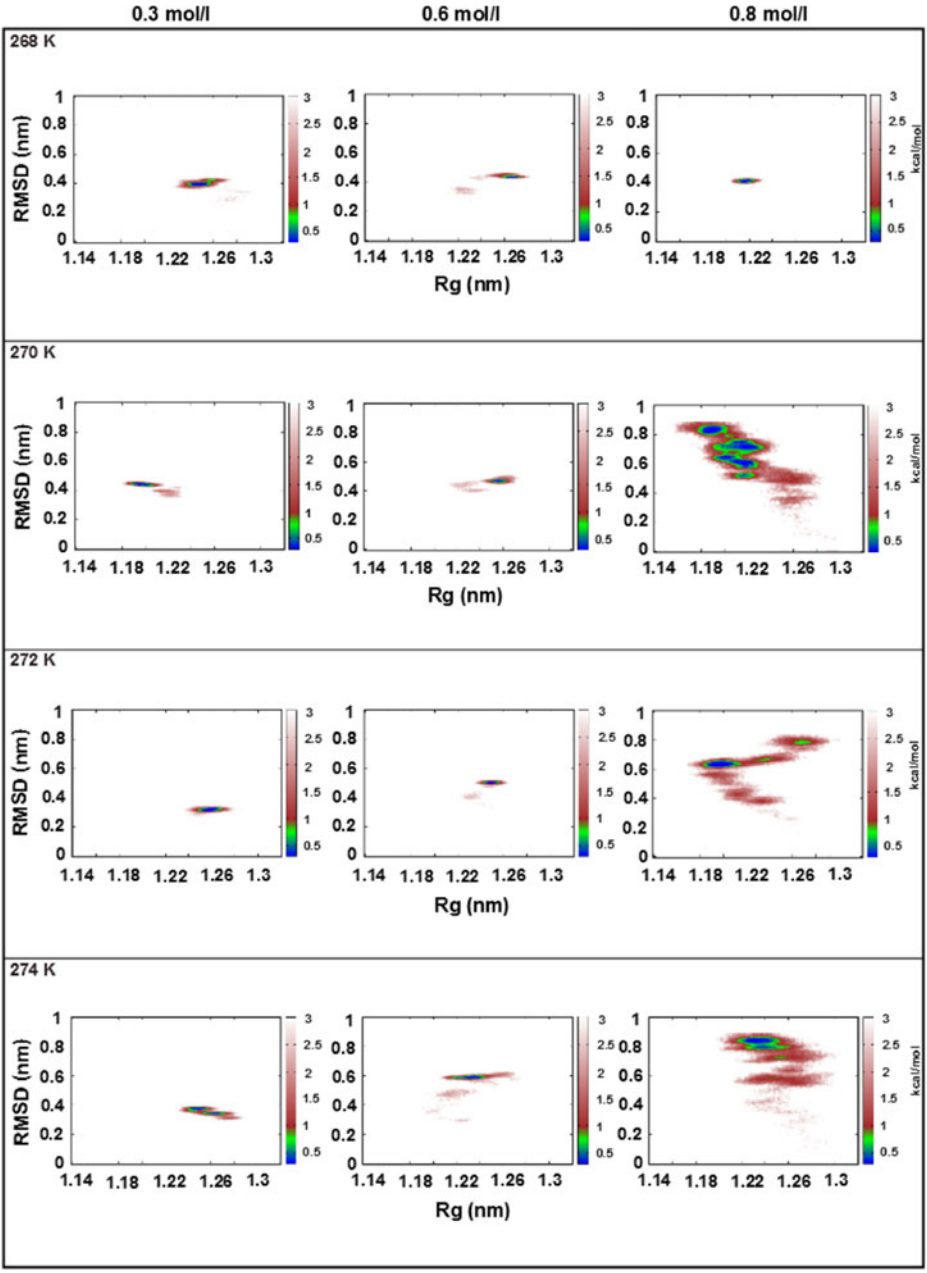

Fig. 4 Free energy landscapes of *Mp*AFP complexes from 268 to 274 K under different NaCl concentrations of 0.3, 0.6, and 0.8 mol/l, plotted as a function of root mean square deviation (RMSD) and radius of gyration (Rg)

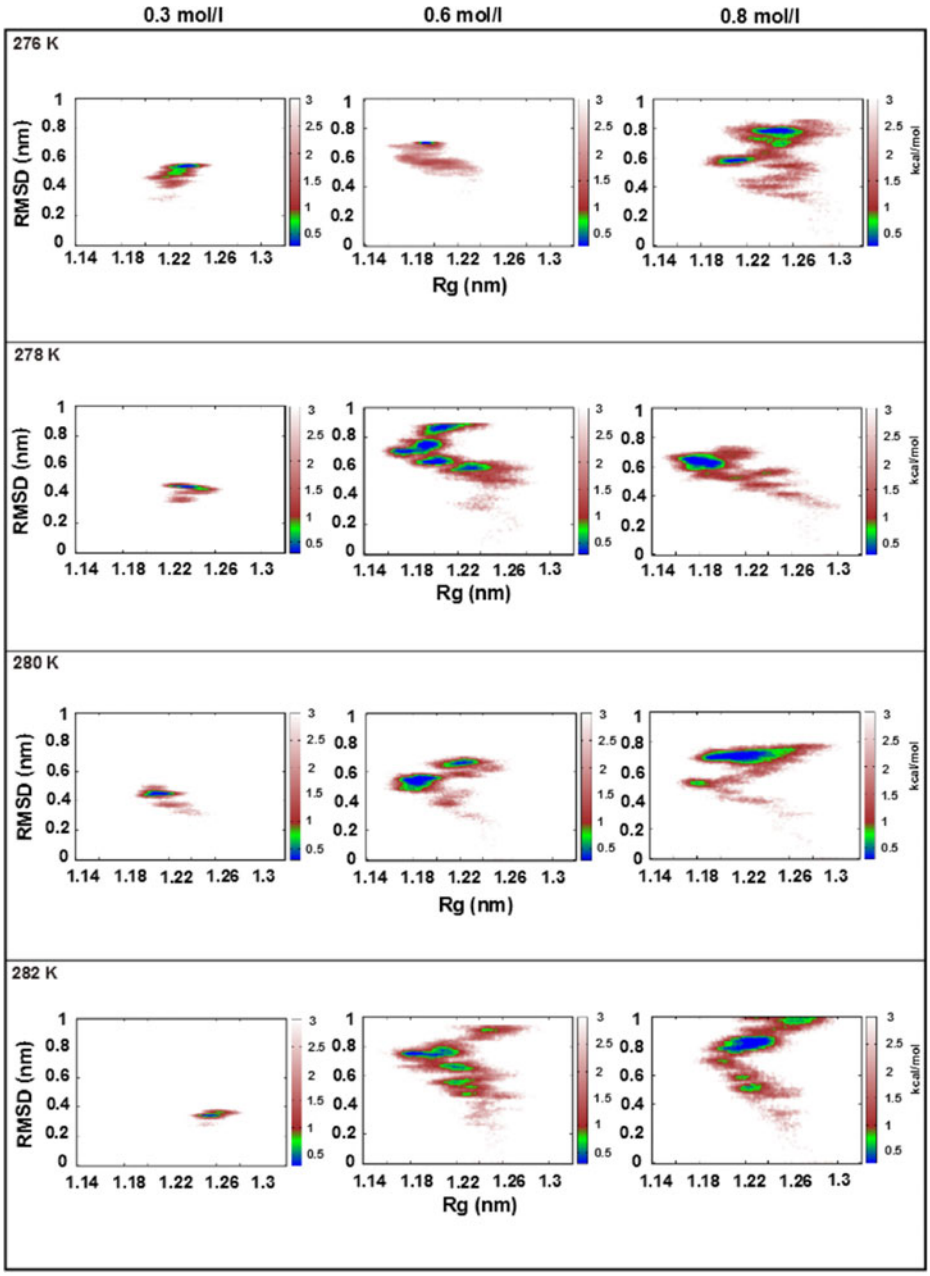

Fig. 5 Free energy landscapes of *Mp*AFP complexes from 276 to 282 K under different NaCl concentrations of 0.3, 0.6 and 0.8 mol/l), plotted as a function of root mean square deviation (RMSD) and radius of gyration (Rg)

(RMSD)). Based on free energy landscape values, we were able to select representative trajectories by identifying the local minimum energy regions of free energy landscapes and also could find out temperature regions that *Mp*AFP remained active. When *Mp*AFP was in ice or ice-liquid hybrid environment, the residues of *Mp*AFP would be inhibited by ice crystal which led to the formation of

limited stable configurations. Therefore, local minimum energy regions are expected to be smaller. In contrast, when *Mp*AFP is in liquid environment, the residues of *Mp*AFP form active configurations which lead to expansion of local minimum energy regions as well as number local minimum energy regions. In detail, Fig. 4 shows free energy landscape of *Mp*AFP in marine environment with various NaCl concentrations of 0.3, 0.6, and 0.8 mol/l from 268 to 274 K. At 268 K, local minimum energy region of *Mp*AFP was discrete. In this case, water molecules surrounding *Mp*AFP were completely frozen; the ice crystal inhibited and paralyzed the *Mp*AFP activity. From 270 to 274 K, the local minimum energy regions of *Mp*AFP were found to be particularly discrete in 0.3 and 0.6 mol/l while that was extended in 0.8 mol/l. Under these temperatures, water molecules formed ice crystal network in both of 0.3 and 0.6 mol/l; and liquid solution in 0.8 mol/l.

The free energy landscapes of *Mp*AFPs under NaCl concentrations of 0.3, 0.6, and 0.8 mol/l from 276 to 282 K were shown in the Fig. 5. At 276 K, with the result of free energy landscape, we found that water molecules surrounding *Mp*AFPs formed ice-liquid hybrid in 0.3 and 0.6 mol/l and liquid solution in 0.8 mol/l; which correspond to the expansion of the local minimum energy regions. From 278 to 282 K, based on local minimum regions, we were able to identify that water molecules surrounding *Mp*AFP formed ice-liquid hybrid in 0.3 mol/l and liquid solution at 0.6 and 0.8 mol/l concentrations.

Conclusions

In this work, we used coarse-grained simulation to study the active *Mp*AFP at low temperatures in combination with different NaCl concentrations. We have found basic behaviors of *Mp*AFP in inhibiting the freezing process of water molecules at low temperatures under various NaCl concentrations. We explored three important findings as follows: (1) the *Mp*AFP could not be active under low NaCl concentration (in 0.3 mol/l) and low temperatures. Under 0.6 mol/l NaCl concentration and the temperatures of equal or greater than 278 K, the *Mp*AFP obtained its active conformation at these subfreezing temperatures. Under 0.8 mol/l NaCl concentration, *Mp*AFP was activated at the temperatures much lower than comparing to the *Mp*AFP in 0.6 mol/l NaCl concentration (the temperatures equal or larger 270 K). Therefore, active temperature region of *Mp*AFP was extended to lower temperatures when NaCl concentration increased. (2) In three cases, the phase transformation of water was found to be dependent on NaCl concentrations, the *Mp*AFP systems allowed us to search for phase space and to locate active conformation in consistent direction than standard single temperature setup. (3) With coarse-grained simulation, the computing expenses were reduced a significant way. However, we also failed to capture some detail information about *Mp*AFP structure; therefore atomistic MD simulation is strongly recommended for further studies.

Acknowledgments The work was funded by the Department of the Navy, Office of Naval Research under grant number N62909-14-1-N234. The computing resources and support provided by Institute for Computational Science and Technology, Ho Chi Minh City, Vietnam are gratefully acknowledged.

References

1. Nguyen, D. T., Colvin, M. E., Yeh, Y., Feeney, R. E., & Fink, W. H. (2002). The dynamics, structure, and conformational free energy of proline-containing antifreeze glycoprotein. *Biophysical Journal, 82*, 2892–2905.

2. Yeh, Y., & Feeney, R. E. (1996). Antifreeze protein: structure and mechanisms of function. *Chemical Reviews, 96*, 601–618.
3. Nguyen, H., Le, L., & Ho, T. B. (2014). Computational study on ice growth inhibition of Antarctic bacterium antifreeze protein using coarse grained simulation. *The Journal of Chemical Physics, 140*, 225101.
4. Raymond, J. A. (2011). Algal ice-binding proteins change the structure of sea ice. *Proceedings of the National Academy of Science of the United State of America, 108*, E198.
5. Janech, M. G., Krell, A., Mock, T., Kang, J. S., & Raymond, J. A. (2006). Ice-binding proteins from sea ice diatoms (Bacillariophyceae). *Journal of Phycology, 42*, 410–416.
6. DeVries, A. L., Komatsu, S. K., & Feeney, R. E. (1970). Chemical and physical properties of freezing point depressing glycoproteins from Antarctic fishes. *The Journal of Biological Chemistry, 245*, 2901–2908.
7. Davies, P. L., Hew, C. L., & Fletcher, G. L. (1980). Fish antifreeze proteins: physiology and evolutionary biology. *Canadian Journal of Zoology, 66*, 2611–2617.
8. Marshall, C. B., Fletcher, G. L., & Davies, P. L. (2004). Hyperactive antifreeze protein in a fish. *Nature, 429*, 153.
9. Worrall, D., Elias, L., Ashford, D., Smallwood, M., Sidebottom, C., Lillford, P., Telford, J., Holt, C., & Bowles, D. (1998). A carrot leucine-rich-repeat protein that inhibits ice recrystallization. *Science, 282*, 115–117.
10. Atici, O., & Nalbantoglu, B. (2003). Antifreeze proteins in higher plants. *Phytochemistry, 64*, 1187–1196.
11. Griffith, M., & Yaish, M. W. F. (2004). Antifreeze proteins in overwintering plants: a tale of two activities. *Trends in Plant Science, 9*, 399–405.
12. Tomchaney, A. P., Morris, J. P., Kang, S. H., & Duman, J. G. (1982). Purification, composition, and physical properties of thermal hysteresis "antifreeze" protein from larvae of the beetle, Tenebrio molitor. *Biochemistry, 21*, 716–721.
13. Hew, C. L., Kao, M. H., So, Y.-P., & Lim, K.-P. (1983). Presence of cystine-containing antifreeze proteins in the spruce budworm, Choristoneura fumiferana. *Canadian Journal of Zoology, 61*, 2324–2328.
14. Schneppenheim, R., & Theede, H. (1980). Isolation and characterization of freezing-point depressing peptides from larvae of Tenebrio molitor. *Comparative Biochemistry and Physiology Part B: Comparative Biochemistry, 67*, 561–568.
15. Duman, J. G., Bennett, V., Sformo, T., Hochstrasser, R., & Barnes, B. M. (2004). Antifreeze proteins in Alaskan insects and spiders. *Journal of Insect Physiology, 50*, 259–266.
16. Robinson, C. H. (2001). Cold adaptation in Arctic and Antarctic fungi. *New Phytologist, 151*, 341–353.
17. Gilbert, J. A., Hill, P. J., Dodd, C. E., & Laybourn-Parry, J. (2004). Demonstration of antifreeze protein activity in Antarctic lake bacteria. *Microbiology, 150*, 171–180.
18. Muryoi, N., Sato, M., Kaneko, S., Kawahara, H., Obata, H., Yaish, M. W. F., Yeh, Y., & Feeney, R. E. (1996). Antifreeze proteins: structures and mechanisms of function. *Chemical Reviews, 96*, 601–618.
19. Meister, K., Ebbinghaus, S., Xu, Y., John, G. D., DeVries, A., Gruebele, M., David, M. L., & Havenith, M. (2012). Long-range protein-water dynamics in hyperactive insect antifreeze proteins. *Proceedings of the National Academy of Science of the United State of America, 110*, 1617–1622.
20. Jorov, A., Zhorov, B. S., & Yang, D. S. (2004). Theoretical study of interaction of winter flounder antifreeze protein with ice. *Protein Science, 13*, 1524–1537.
21. Braslavsky, I., & Drori, R. (2013). LabVIEW-operated novel nanoliter osmometer for ice binding protein investigations. *Journal of Visualized Experiments, 72*, e4189.
22. Chattopadhyay, M. K. (2007). Antifreeze proteins of bacteria. *Resonance, 12*, 25–30.
23. John, G. D., & Olsen, T. M. (1993). Thermal hysteresis protein activity in bacteria, fungi and phylogenetically diverse plants. *Cryobiology, 30*, 322–328.
24. Fletcher, G. L., Hew, C. L., & Davies, P. L. (2001). Antifreeze proteins of teleost fishes. *Annual Review Physiology, 63*, 359–390.
25. Davies, P. L., Baardsnes, J., Kuiper, M. J., & Walker, V. K. (2002). Structure and function of antifreeze proteins. *Philosophical Transactions of the Royal Society of London. Series B, Biological Sciences, 357*, 927–935.
26. Christopher, P. G., Robert, L. C., & Peter, L. D. (2011). Anchored clathrate waters bind antifreeze proteins to ice. *Proceedings of the National Academy of Science of the United State of America, 108*, 7363–7367.
27. Devries, A. L., & Lin, Y. (1977). Structure of a peptide antifreeze and mechanism of adsorption to ice. *Biochimica et Biophysica Acta, 495*, 388–392.
28. Chao, H., Houston, M. E., Jr., Hodges, R. S., Kay, C. M., Sykes, B. D., Loewen, M. C., Davies, P. L., & Sönnichsen, F. D. (1997). A diminished role for hydrogen bonds in antifreeze protein binding to ice. *Biochemistry, 36*, 14652–14660.
29. Baardsnes, J., Kondejewski, L. H., Hodges, R. S., Chao, H., Kay, C., & Davies, P. L. (1999). New ice-binding face for type I antifreeze protein. *FEBS Letters, 463*, 87–91.
30. Nutt, D. R., & Smith, J. C. (2008). Dual function of the hydration layer around an antifreeze protein revealed by atomistic molecular dynamics simulations. *Journal of the American Chemical Society, 130*, 13066–13073.

31. Gallagher, K. R., & Sharp, K. A. (2003). Analysis of thermal hysteresis protein hydration using the random network model. *Biophysical Chemistry, 105*, 195–209.
32. Smolin, N., & Daggett, V. (2008). Formation of ice-like water structure on the surface of an antifreeze protein. *The Journal of Physical Chemistry B, 112*, 6193–6202.
33. Wierzbicki, A., Dalal, P., Cheatham, T. E., 3rd, Knickelbein, J. E., Haymet, A. D., & Madura, J. D. (2007). Antifreeze proteins at the ice/water interface: three calculated discriminating properties for orientation of type I proteins. *Biophysical Journal, 93*, 1442–1451.
34. Yang, C., & Sharp, K. A. (2004). The mechanism of the type III antifreeze protein action: a computational study. *Biophysical Chemistry, 109*, 137–148.
35. Yang, C., & Sharp, K. A. (2005). Hydrophobic tendency of polar group hydration as a major force in type I antifreeze protein recognition. *Proteins, 59*, 266–274.
36. Garnham, C. P., Campbell, R. L., & Davies, P. L. (2011). Anchored clathrate waters bind antifreeze proteins to ice. *Proceedings of the National Academy of Science of the United State of America, 108*, 7363–7367.
37. Guo, S., Garnham, C. P., Partha, S. K., Campbell, R. L., Allingham, J. S., & Davies, P. L. (2013). Role of Ca^{2+} in folding the tandem β-sandwich extender domains of a bacterial ice-binding adhesion. *FEBS Journal, 280*, 5919–5932.
38. Humphrey, W., Dalke, A., & Schulten, K. (1996). VMD-visual molecular dynamics. *Molecular Graphics, 14*, 33–38.
39. Siewert, J. M., Risselada, H. J., Yefimov, S., Tieleman, D. P., & Alex, H. D. (2007). The MARTINI force field: coarge grained model for biomolecular simulation. *The Journal of Physical Chemistry B, 111*, 7812–7824.
40. Le, L., & Molinero, V. (2011). Nanophase segregation in supercooled aqueous solutions and their glasses driven by the polyamorphism of water. *The Journal of Physical Chemistry. A, 115*, 5900–5907.
41. Hess, B., Kutzner, C., van der Spoel, D., & Lindahl, E. (2008). GROMACS 4: algorithms for highly efficient, load-balanced, and scalable molecular simulation. *Journal of Chemical Theory and Computation, 4*, 435–447.
42. Darden, T., York, D., & Pedersen, J. (1993). Particle mesh Ewald: an Nlog (N) method for Ewald sums in large systems. *The Journal of Chemical Physics, 98*, 10089–10092.
43. Yesylevskyy, S. O., Schäfer, L. V., Sengupta, D., & Marrink, S. J. (2010). Polarizable water model for the coarse-grained MARTINI force field. *PLoS Computational Biology, 6*, e1000810.
44. Kar, R. K., & Bhunia, A. (2015). Biophysical and biochemical aspects of antifreeze proteins: using computational tools to extract atomistic information. *Progress in Biophysics and Molecular Biology, 119*, 194–204.
45. Kar, R. K., & Bhunia, A. (2015). Will it be beneficial to simulate the antifreeze proteins at ice freezing condition or at lower temperature? *The Journal of Physical Chemistry B, 119*, 11485–11495.
46. Sanz, E., Vega, C., Abascal, J. L. F., & MacDowell, L. G. (2004). Phase diagram of water from computer simulation. *Physical Review Letters, 92*, 255701.
47. Kofke, D. A., & Post, A. J. (1993). Hard particles in narrow pores. Transfer-matrix solution and the periodic narrow box. *The Journal of Chemical Physics, 98*, 1331–1336.
48. Berendsen, H. J. C., Postma, J. P. M., Gunsteren, W. F. V., Dinola, A., & Haak, J. R. (1984). Molecular dynamics with coupling to an external bath. *The Journal of Chemical Physics, 81*, 3684–3690.
49. Parrinello, M., & Rahman, A. (1981). Polymorphic transitions in single crystals: a new molecular dynamics method. *Journal of Applied Physics, 52*, 7182–7190.
50. Hockney, R. W., Goel, S. P., & Eastwood, J. (1974). Quit high resolution computer models of plasma. *Journal of Computational Physics, 14*, 148–158.
51. Mu, Y., Nguyen, P. H., & Stock, G. (2005). Energy landscape of a small peptide revealed by dihedral angle principal component analysis. *Proteins, 58*, 45–52.
52. Nguyen, H., Van, T. D., & Le, L. (2015). Coarse grained simulation reveals antifreeze properties of hyperactive antifreeze protein from Antarctic bacterium Colwellia sp. *Chemical Physics Letters, 638*, 137–143.
53. Wang, Y., Teitel, S., & Dellago, C. (2005). Melting of icosahedral gold nanoclusters from molecular dynamics simulations. *The Journal of Chemical Physics, 122*, 214722.